JATIS Journal of Astronomical Telescopes, Instruments, and Systems

RESEARCH PAPER

Science application driven optimization of LSSTCam charge-coupled device clocking

Anthony Tyson,[a,*] Adam Snyder,[a] Craig Lage,[a] Daniel Polin,[a] Gregg Thayer,[b] Stuart Marshall,[b] Yousuke Utsumi,[b,c] Tony Johnson,[b] and Max Turri[b]

[a]University of California, Department of Physics and Astronomy, Davis, California, United States
[b]SLAC National Lab, Menlo Park, California, United States
[c]National Astronomical Observatory of Japan, Tokyo, Japan

ABSTRACT. We outline the scientific motivation for reducing the systematics in the image sensors used in the LSST. Some examples are described, leading to lab investigations. The CCD250 (Teledyne-e2v) and STA3900 Imaging Technology Laboratory (ITL) charge-coupled devices (CCDs) used in Rubin Observatory's LSSTCam are tested under realistic LSST f/1.2 optical beam in a lab setup. In the past, this facility has been used to characterize these CCDs, exploring the systematic errors due to charge transport. Now, this facility is being used to optimize the clocking scheme and voltages. The effect of different clocking schemes on the on-chip systematics such as non-linear crosstalk, noise, persistence, and photon transfer is explored. The goal is to converge on an optimal configuration for the LSSTCam CCDs, which minimizes resulting dark energy science systematics.

Keywords: charge-coupled device sensors; Rubin Observatory; LSST; dark energy; charge-coupled device clocking; charge-coupled device systematics

Paper 24098SS received Jul. 8, 2024; revised Aug. 23, 2024; accepted Aug. 23, 2024; published Oct. 26, 2024.

1 Introduction

The charge-coupled devices (CCDs) that are used in the Rubin Observatory camera (LSSTCam) are a special design, dictated by the rapid pace across the sky of the imaging survey: LSST.[1] Driven by the prospect of imaging billions of distant galaxies many hundreds of times, the large telescope–camera system was designed to take short exposures and read out all 3.2 billion pixels in only 2 s. One thousand to 2000 exposures will be made per night for 10 years.

In this brief paper, we describe how two of the science motivations for LSST (dark energy and dark matter) drove the CCD design and discuss the low-level systematics of the sensor which must be minimized for LSST to reach its science potential. Past sky surveys have been sample-limited (generating a statistical noise), but our system collects so much light and covers such a large area per exposure that we will not be sample-limited: the LSST science will be systematics-limited. Some of those systematics are astrophysical, and some systematics come from the atmosphere, but the overall systematic error cannot be smaller than those systematics arising in the CCD sensors.

Dark matter and dark energy (the late-time acceleration of the expansion of the universe) comprise 95% of the mass energy of our universe and are evidence of new physics—beyond the standard model of particle physics. The prospect of probing them with LSST is exciting.

*Address all correspondence to Anthony Tyson, tyson@physics.ucdavis.edu

We begin by describing one of the LSST probes of the characteristics of dark energy and dark matter (weak gravitational lensing and the associated "cosmic shear") and show how the requirements for precision dark energy science lead to requirements for precision in the CCD signal.

2 Cosmology Drives Sensor Design

Figure 1 shows a view through the three-dimensional (3D) universe similar to what we expect from LSST. This simulated color image,[2] a composite of three individual frames with different color filters, shows one 4 K × 4 K CCD (13 × 13 arcmin of the sky) out of 189 CCDs in the LSST focal plane. It corresponds to only 2.6 parts per million of LSST's ultimate sky coverage of 20,000 square degrees. We see a few foreground stars, several foreground galaxies, and an abundance of very distant galaxies.

Those distant galaxies are also distributed over a wide range of distance and redshift z, with most of them between redshift 0.5 and 3. This enables probes of the nature of space time in that large volume, using those galaxies' apparent location and shapes as signposts.

Light from a distant galaxy passes by over-densities of dark matter on its way to us, deflecting its rays. The distant galaxies thus appear at new places in the sky, and their shape is distorted into a miniature arc: a cosmic mirage. An intrinsically round galaxy will be distorted into an elliptical shape with a major to minor axis ratio a/b. For faint galaxy weak lensing, the dimensionless galaxy shear γ is defined in terms of an amplitude $|\gamma| = (1 - b/a)/(1 + b/a)$ and a direction. Correlations of shear among pairs of galaxies as a function of redshift enable sensitive probes of the nature of dark matter and dark energy.

This effect is shown in Fig. 2 in which the distortions of galaxies in different parts of the sky trace out the intervening dark matter. This important cosmological tool is called "cosmic shear." The positions and shapes of pairs of galaxies at different sky separations, as a function of redshift, encode the underlying cosmological parameters as a function of look-back time.

The prospect of tracing the development of dark matter structure as well as dark energy (the recent acceleration of the expansion of the universe) over cosmic time has been a key science driver for LSST from the earliest days of the project.[1,3–5] First detected in 2000,[6–9] the cosmic shear signal is small: a coherent distortion of background galaxies with a shear of typically 0.002 on tens of arcminute scales. To measure this at the S/N needed for precision cosmology,

Fig. 1 Looking through a 3D universe. This simulation of a small part of the sky as seen by Rubin Observatory's LSST shows some foreground stars and many background galaxies.

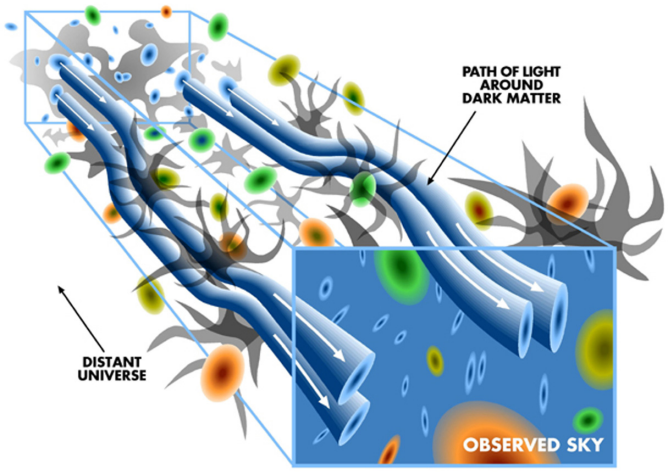

Fig. 2 Looking back to galaxies in the early universe and their shape distortions as their light passed by different over-densities of dark matter on its way to us. Using this "cosmic shear," we can make maps of dark matter as a function of redshift at all sky locations covered by LSST. However, the point spread function must be known.

systematics must be kept below 0.0001 shear. This competes with atmospheric and instrumental effects including the point spread function (PSF) which are orders of magnitude larger. There is a correction needed for the shear amplitude which must be kept below 0.001 to achieve this shear precision.

Methods for addressing this are discussed below. There are several interlocking weak lens probes of cosmic structure, so-called 3×2 point correlations, which reduce degeneracies. We utilize several types of two-point correlation functions in LSST data: galaxy clustering for position–position correlation, galaxy–galaxy lensing for position–shear correlation, and cosmic shear for shear–shear correlation. These depend differently on the so-called mass bias. Combinations of pairs of these correlation functions can avoid this bias, yielding a relatively clean probe of dark matter and dark energy as a function of redshift.[10,11]

An even more powerful technique is to combine these LSST probes with cosmic microwave background (CMB) spectral measurements. Combining LSST lensing data with CMB lensing is particularly powerful.[12,13]

To detect this cosmic shear, we must calibrate the optical aberration PSF to better than 100 ppm. Both cosmological dark matter and the atmosphere above the telescope can shear galaxy images. We use stars in the same field of view, and in exposures taken at the same time, to measure the telescope–atmosphere PSF and thus calibrate the shear. This process is shown in Fig. 3. A single galaxy is sheared by 10%, for visualization purposes. In reality, the cosmic shear is a factor of 100 smaller. So, the ellipticity of many galaxies must be averaged in a given patch of sky to detect this small signal. Moreover, galaxies are not all round—they come in a wide variety of shapes. This ellipticity sample noise is typically a root mean square (rms) faint galaxy ellipticity of 0.2. Thus, this cosmic signal is 100 times smaller. Although statistical errors average down with the number of exposures, generally systematic errors do not. We must have enough galaxies in the sample to reach the statistical error floor where systematic errors play a role. To reach a shear systematics precision of 0.0001, we must have a sample of thousands of galaxies per 10-arcmin-wide sky patch.

As most of the cosmic shear signal is on angular scales of 10 arcmin and less, we require a sample of ~40 faint galaxies per square arcminute. This yields a requirement for a so-called gold sample of several billion faint galaxies.[1] This requirement, among others, led to the large aperture of LSST and its large focal plane.

The precision needed in faint galaxy shear measurement calls for special effort in theoretical modeling of astrophysical systematics,[14,15] as well as hardware and observing techniques for mitigating the residual shear systematics in the data.[16,17] In the end, the data can be no better than the residual systematics generated in the camera. Dithering of exposures on a sky patch can help reduce some systematics. Rotating the field can break degeneracies and is a powerful tool.

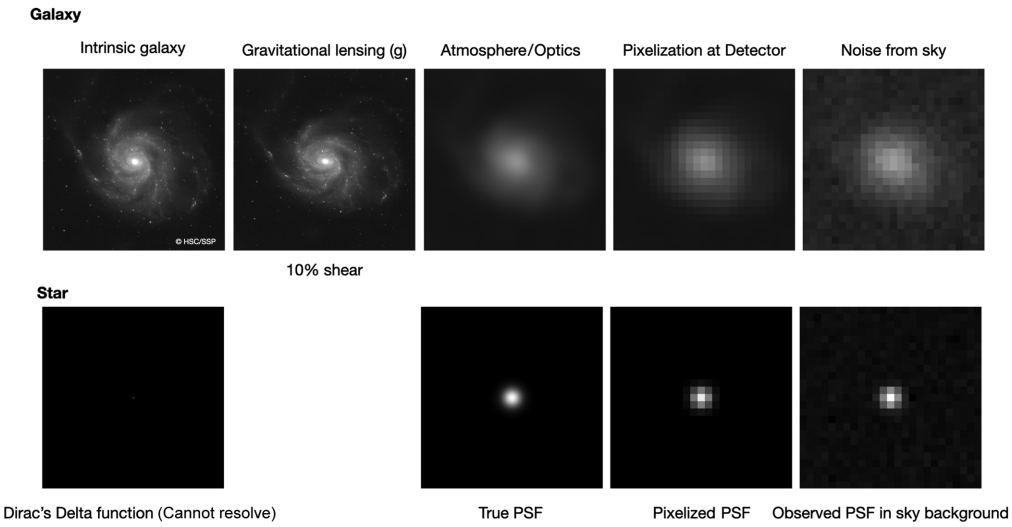

Fig. 3 The galaxy shear must be calibrated using the known PSF from stars in the same field of view. This cartoon shows the process of shear and its calibration. A population of stars in each exposure is used to define the PSF in that exposure. The shear in this figure is exaggerated for visualization. The actual cosmic shear is a factor of 100 smaller, and we must calibrate the PSF ellipticity to a precision 10 times smaller than that. The current generation of shear surveys has not reached the precision required for LSST, but new techniques hold some promise.[13,14]

Any delivered PSF ellipticity in a field becomes randomized in direction after combining many exposures, each with a different camera rotation.

From the earliest days of the project over 20 years ago, it was planned to have an instrument rotator. This is needed due to slow field rotation during exposures because we have an altitude-azimuth (ALT-AZ) telescope. It is also required for the purpose of mitigating residual PSF ellipticity, and an updated design was produced 10 years ago at the official start of construction.[18] Residual shear systematics integrate down over hundreds of exposures in a sky patch. Bright star diffraction spikes are also eliminated because they rotate over the ~100 visits to a field in each filter. These measures mitigate against cosmological systematics (bogus galaxies) as well as time–domain bogus alerts. Figure 4 shows the position of the LSST instrument rotator relative to the rest of the LSSTCam.

To fully cover the required range of 180 deg (PSF relative to North), the rotator is designed to cover ±90 deg. Combined with the proper observing strategy, this can optimally reduce the

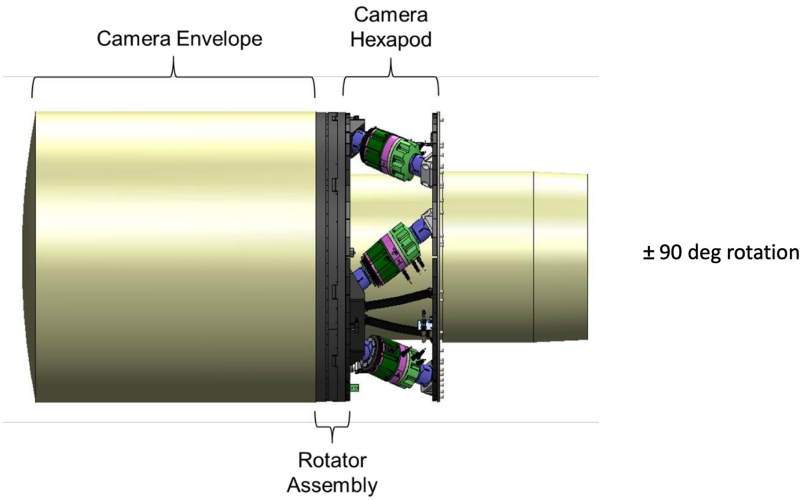

Fig. 4 The LSSTCam can be rotated ±90 deg around its axis. Over thousands of exposures, this can average down the net PSF ellipticities and thus mitigate the residual shear systematics.

effects of residual shear for the measurement of cosmological parameters based on weak lens data.[19]

3 Sensor Design and Requirements

To cover the sky rapidly, the entire focal plane must be read out in a time that is short compared with the individual exposures. Due to the large telescope aperture, a single 15-s exposure can reach 24th magnitude. Slewing the telescope to a new sky position takes an average of 5 s, during which the CCD may be read out. It was decided early that a nominal 2-s readout time would be ideal. As a result, the LSSTCam focal plane is highly segmented, consisting of 189 4 K × 4 K fully depleted back-illuminated silicon CCDs. Several considerations led to a focal plane populated by relatively small CCDs, each highly segmented.[20,21] Figure 5 shows the focal plane layout and a zoom-in to one of the 16-segment CCDs.

Synchronous clock signals are fed to the CCDs, and all 16 segments of the CCD are simultaneously read out through their own output amplifier. Note that the eight amplifiers within each half of the CCD read out in opposite parallel directions from the mid-line up and from the mid-line down; this will play a role in crosstalk systematics (discussed below).

The resulting 3024 video signals are fed via ribbon cables to an electronics module directly behind the CCD. The CCDs are grouped in units of 9; thus, we have 21 so-called rafts of 3 × 3 groups of CCDs. Low noise was another consideration that led to small segments: pixel read rates of less than 1 Mpix per second, combined with a 2-s readout. Typical *r* band night sky levels of 1000 electrons per pixel in a 15-s exposure (30 electrons rms sky noise) led to the requirement of read noise less than ∼10 electrons rms which is achievable at 0.5 Mpix per second. The CCD read noise is then subdominant to the rms sky noise. With these red response, speed, and noise requirements, each vendor was free to design their own fabrication process and readout architecture. The architectures of the two CCDs are very different.[22] The Imaging Technology Laboratory (ITL) design is much more effective at eliminating holes captured in the imaging region. We think this accounts for the difference in persistence, but we are not certain. Neither vendor has provided clues.

4 CCD Systematics and Lab Testing

A leading systematic error that impacts the LSST weak lensing PSF calibration is due to charge transport in the silicon. This affects both the ITL and Teledyne-e2v CCDs and is independent of the readout electronics. The brighter–fatter (BF) effect in CCDs[23–25] due to charge drift,

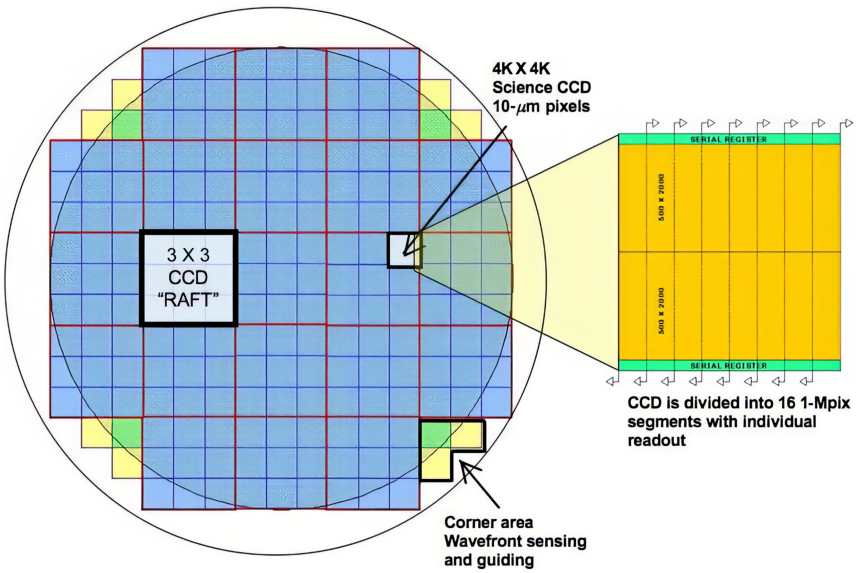

Fig. 5 Each of the 189 4 K × 4 K CCDs is split into 16 segments, each with its own output amplifier.

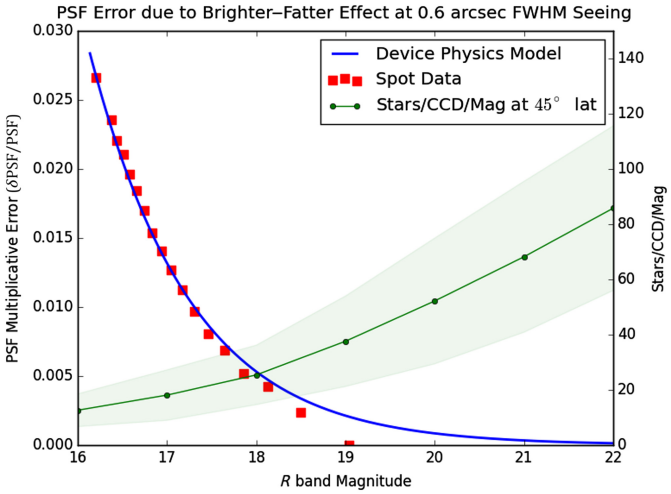

Fig. 6 Laboratory measurements using the $f/1.2$ LSST beam simulator, addressing PSF calibration. This plot shows the lab-generated data for effects on PSF ellipticity due to the brighter–fatter effect (left axis) and the number of stars in the CCD field (right axis) versus their brightness.

diffusion, and space charge spreading in the last few microns of the CCD impacts LSST science. The detailed sub-pixel shapes of star images[26] have been studied using the $f/1.2$ beam simulator (discussed below). The BF effect has a PSF ellipticity component due to the charge confinement of the channel stops: charge from a bright star spreads more easily parallel to the channel stops. This effect is shown in Fig. 6. The BF effect on star ellipticity (left axis) is shown, whereas the right axis gives the number of stars per LSST CCD in a typical survey exposure. Brighter stars are more elliptical. Fainter stars can be confused with compact galaxies and have low S/N. A typical brightness range of selected PSF stars may result in a net PSF ellipticity of 0.002; this error is an order of magnitude larger than the goal. The goal is to deduce the PSF appropriate for the faint galaxies, not the bright stars. Thus, a correction for this BF-induced PSF ellipticity effect must be made. A facility for projecting a realistic scene of stars and galaxies onto the CCD is useful for validating such algorithms.

The LSST beam simulator at UC Davis[27] is a wide field nearly 1:1 re-imaging system that produces the centrally obscured $f/1.2$ optical beam of the LSST Camera. It can illuminate a single CCD with realistic astronomical scenes. The input and output port has a wide 60-mm diameter image field. A mask at the input port is re-imaged onto the CCD. The PSF of the system is 4 μm, which is 12 times smaller than the typical delivered PSF by the atmosphere. The test stand (Fig. 7) consists of a large integrating sphere, the optical re-imager assembly, focal plane shutter, and a single CCD cryostat mounted on a programmable three-axis mechanical stage that allows for adjustment of the azimuth and polar angles.

These images allowed us to calculate standard electro-optical properties including the gain, read noise, and dark current. Each property was calculated on a per-segment basis. Due to the high dimensionality of voltage, timing, and clocking search space, a small fraction of data was ultimately saved. The decision was based on an examination of test results and observation of trends. To increase precision, hundreds of repeat runs were taken at these sparse configurations.

There are two cryostats available for installation and testing, one containing an ITL STA3800 CCD and one containing a Teledyne-e2v CCD250. A fog of incoherent photons exits the integrating sphere and enters the input port of the re-imager optics. A ray trace diagram of the re-imager optics is shown in Fig. 8. Optical LSSTCam bandpass filters covering the g, r, i, z, y bands and photolithographic source masks can be installed independently at the re-imager input port either to provide flat field illumination or to illuminate the CCD with a realistic astronomical scene. There is a provision for injecting light in the pupil plane for separate sky illumination, either a flat spectrum or a custom spectrum derived from a monochromator.

Ribbon cables bring the CCD clocking signals and the video output signals to external digital and analog electronics. The signal processing electronics use the same custom-designed REB5 circuit board used in the main camera. The data acquisition system interfaces with the

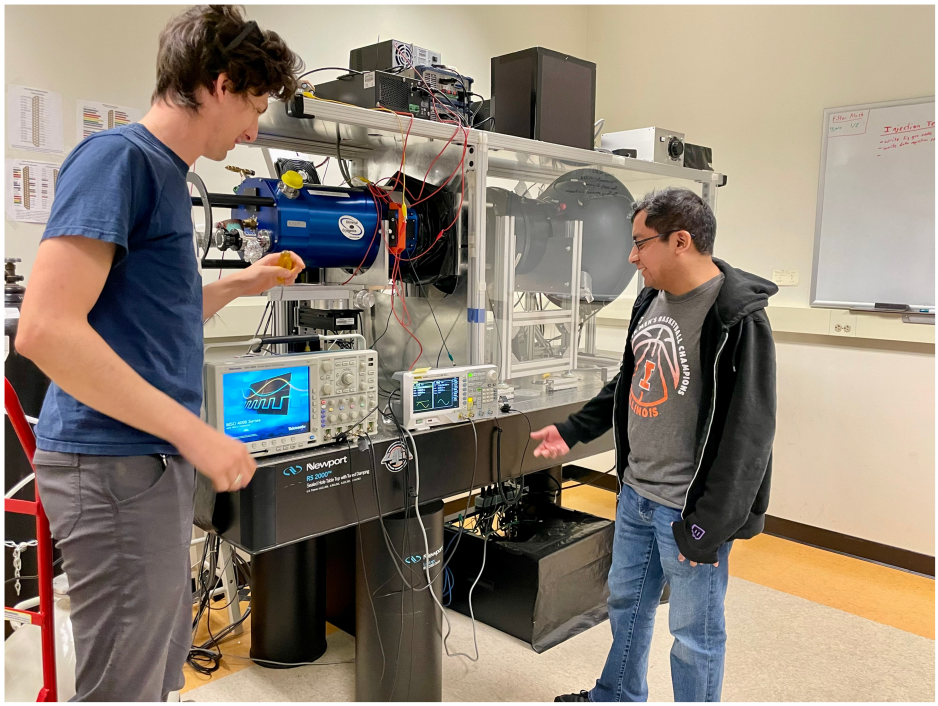

Fig. 7 Daniel Polin and Adam Snyder are shown in the beam simulator lab. The LSST beam simulator consists of an integrating sphere (right), optical assembly (middle), and the CCD cryostat (left) supported by a three-axis mechanical stage. This allows "dithering" of images and automated focusing.

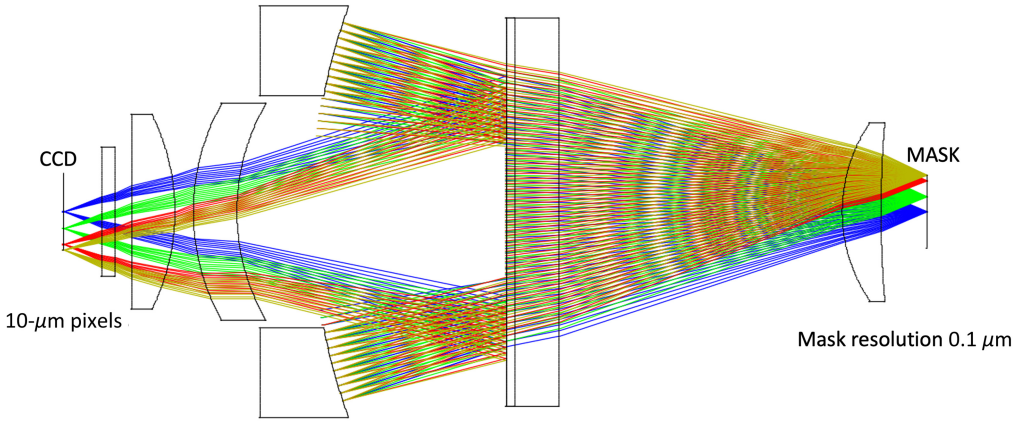

Fig. 8 LSST beam simulator optics. A 60-mm diameter input and output image field enables the illumination of an entire CCD with an $f/1.2$ beam identical to that of LSST.

REB5 via an optical transition module. Finally, a version of the Rubin Camera Control System software was installed on the lab computer. Data from the LSST beam simulator are fully compatible with the LSST Science Pipelines developed by Rubin Data Management. This is accessible through a Data Butler[28] repository located at the LSST Data Facility (USDF) hosted by the SLAC National Accelerator Laboratory (SLAC).

4.1 CCD Clocking Optimization

Our exploration of LSST CCD systematics relies on the changes in clocking voltages and timings. Correlated double sampler ramp and buffer timings are varied. This yielded hints for the origin of some systematics. It is useful to narrow down the origin of the systematic; does it arise in the CCD chip or in the REB5 readout electronics? In addition to studies of the effect on images produced by the CCD, we also replace the CCD with a proxy. By injecting a replica of the CCD

video output pulse into the REB5, we gain an understanding of the origin of crosstalk and other systematics. We also adjust the phases of the clocking in a series of experiments. Changing the parallel transfer clocking scheme from one that uses overlapping parallel clocks (nominal) to one that uses non-overlapping parallel clocks affects bright star persistence in the Teledyne-e2v CCD. The overlapping parallel transfer was introduced to increase parallel transfer efficiency and full well. On the other hand, one single-phase transition between high and low states where three parallel clocks overlap could cause accumulated charges to become trapped at the interface layer, creating trailing persistence. Some of these results are briefly mentioned below.

4.2 Crosstalk, Linear, and Non-Linear

With our highly segmented CCD, low-level electronic crosstalk occurs among pairs of sub-channels. The signal of a bright source object in one segment generates "ghost" objects in the other segments. The focal plane for the LSST camera has crosstalk that occurs at various locations in the signal chain: the initial on-chip amplification, on the flex cables that connect the CCD to the REB5, and within the various components of the REB5.[29] Both linear and non-linear crosstalk among the 16 video outputs are seen in both ITL and Teledyne-e2v LSST CCDs.

A bright star will have a ghost image in another segment at a position that corresponds to the instant that the charge enters the output amplifier on the bright star's segment. Dithering subsequent exposures in either X or Y unfortunately results in the ghost star appearing in the same relative position, so that co-adding a series of dithered exposures will not mitigate this ghost star. However, if the field is rotated among exposures, then the crosstalk ghost star moves its relative position,[30] and a median average co-add of many exposures will not contain the crosstalk ghost. As a given sky patch will be revisited many times at different telescope RA, the field will naturally rotate on the CCD camera over a wide range of angles in 10 years. However, bad seeing on some visits can be addressed by targeted revisits which will require occasional large camera rotations. To fully average down the CCD-based galaxy ellipticity systematics, the field should be rotated by a large angle whenever a field is revisited. This can only be done when the camera is horizontal, which will not occur frequently. As the current plan is to rotate the camera by large angles occasionally, this mitigation will not be perfect.

Not all bright objects are fixed at known positions in the sky. A bright streak caused by a satellite passing through the field of view during integration will act as a source object that can affect a large area of the focal plane due to crosstalk ghost streaks. To simulate a satellite streak, a lithographic mask consisting of a 40-μm-wide slit spanning the full CCD was installed and reimaged by the LSST beam simulator to form a streak with a full width at half maximum of $\sim$4 pixels. The xyz stage enables positional dithering of the streak. Figure 9 is an example raw image of the projected streak showing the streak profile and the resulting crosstalk response on the full 4 K $\times$ 4 K CCD.

The crosstalk for each segment pair is on the order of 10^{-3} for our setup at UC Davis and is non-linear with intensity: crosstalk varies by up to 20% over the range of normal illumination. The linear term in crosstalk for the LSSTCam is about five times lower, due to shorter video cables. The correction algorithm requires the use of both a linear and a first-order non-linear crosstalk term to reduce the residuals to below 1 electron per pixel across the full range of source signal values. These 16×16 crosstalk matrices (one for each of the 189 science CCDs in LSSTCam) must be characterized for each of the 189 science CCDs in the Rubin LSST Camera. Not all matrix elements are significant. There are typically 2300 significant matrix elements. To calibrate these on-sky, we will make use of $\sim$10 to 20 relatively bright stars per square arcminute with a good S/N ratio. About 50 exposures, each with their own 2300 matrix elements, must be averaged. Multiplying by the number of significant segment-segment crosstalk pairs per CCD and the sky area per CCD, we have over a million crosstalk matrix elements that must be calibrated on-sky. This could be achieved in monthly twilight campaigns.

4.3 Bright Image Persistence

LSST exposures will include bright stellar images that exceed the saturation point of the CCD imagers. Even in fully depleted silicon, under some operating conditions, it is possible for charge to reach the $Si - SiO_2$ interface at the CCD "surface" and become trapped. Subsequent inversion of the surface can provide holes with which these trapped electrons recombine.[31]

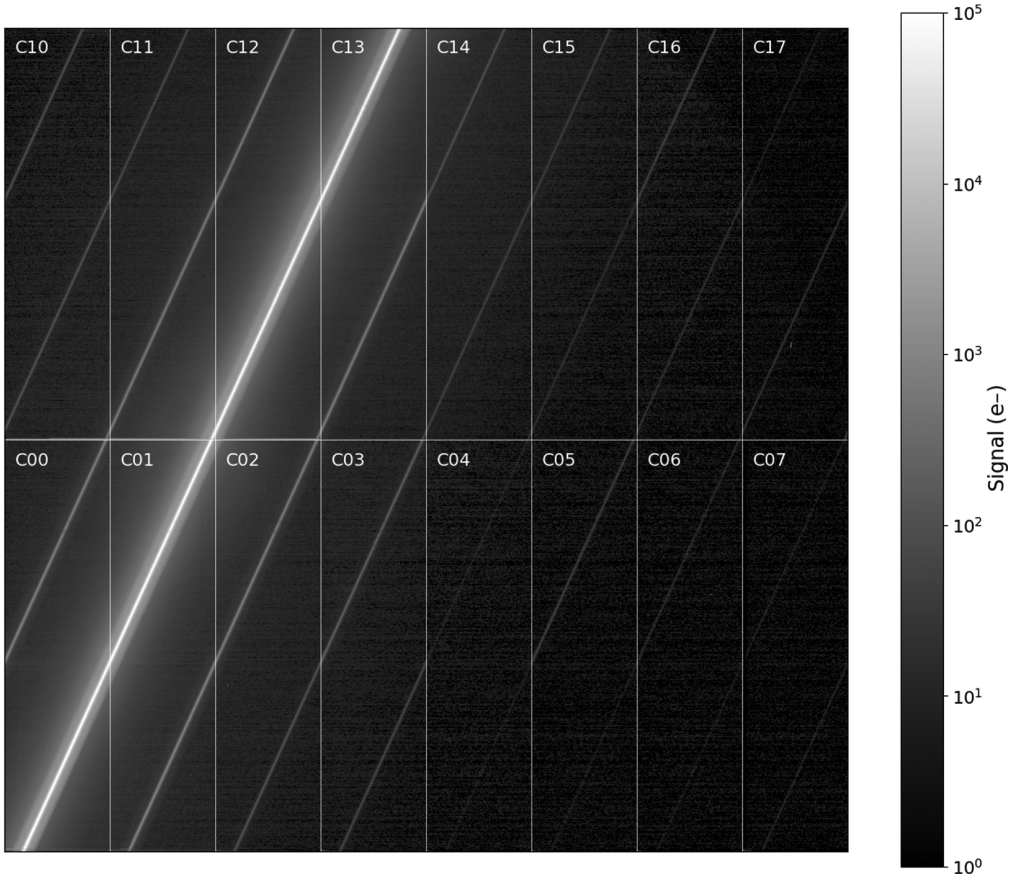

Fig. 9 Crosstalk in a LSST Teledyne-e2v CCD. All 16 segments (annotated with white lines and segment names) are shown. A satellite streak image is projected onto four amplifier segments by the LSST beam simulator. The induced crosstalk signals in other amplifiers are shown as echoes in the same pixel location as the central streak in the source amplifier. The intensity stretch is on a log scale, spanning one electron to saturation.

Spot imaging was performed using an LSST-like cadence. Using the $f/1.2$ beam simulator, the residual charge was measured as a function of subsequent exposure number and parallel clock voltages. Although the ITL CCDs do not show any residual image "persistence," even after exposure at many times saturation, the Teledyne-e2v CCDs do show this behavior. This is shown in Fig. 10. A projected spot near saturation in the previous exposure (left) exhibits persistence (right) in a subsequent 15-s dark exposure. Typical time scales for the decay of this persistence is tens of seconds. The effect depends on voltages and clock timings. We study this persistence as a function of parallel clock high/low voltages and clock timing schemes in a high-dimensional characterization matrix.

The effect was originally discovered by Peter Doherty in e2v LSST prototype CCDs operating with unipolar clocks.[32] He found that the persistence decreased with decreasing parallel clock-high. In our recent testing using bipolar clocks, we similarly find a decrease in persistence with decreasing parallel clock-high and clock-low (keeping the swing constant). One interpretation is that this voltage condition lets excessive charges flow along the column direction before it reaches the surface layer by reducing the full well (or creating a surface full well condition.)

These observations are consistent with the idea of charges being trapped at the $Si-SiO_2$ interface. The initial recommendations for the Teledyne-e2v devices were all parallel rail voltages positive (unipolar; parallel high at $+9$ V and low at 0 V). To remove flat image distortion called "tearing," we brought the voltages down to $+3.3$ and -6 V.[33] By contrast, the ITL voltage swing is $+2$ and -8 V. The voltages for two different vendors are close now. However, the difference is whether the voltage is low enough to establish the pinning condition. This is probably the key difference in whether the CCD develops a condition called "pinning" where

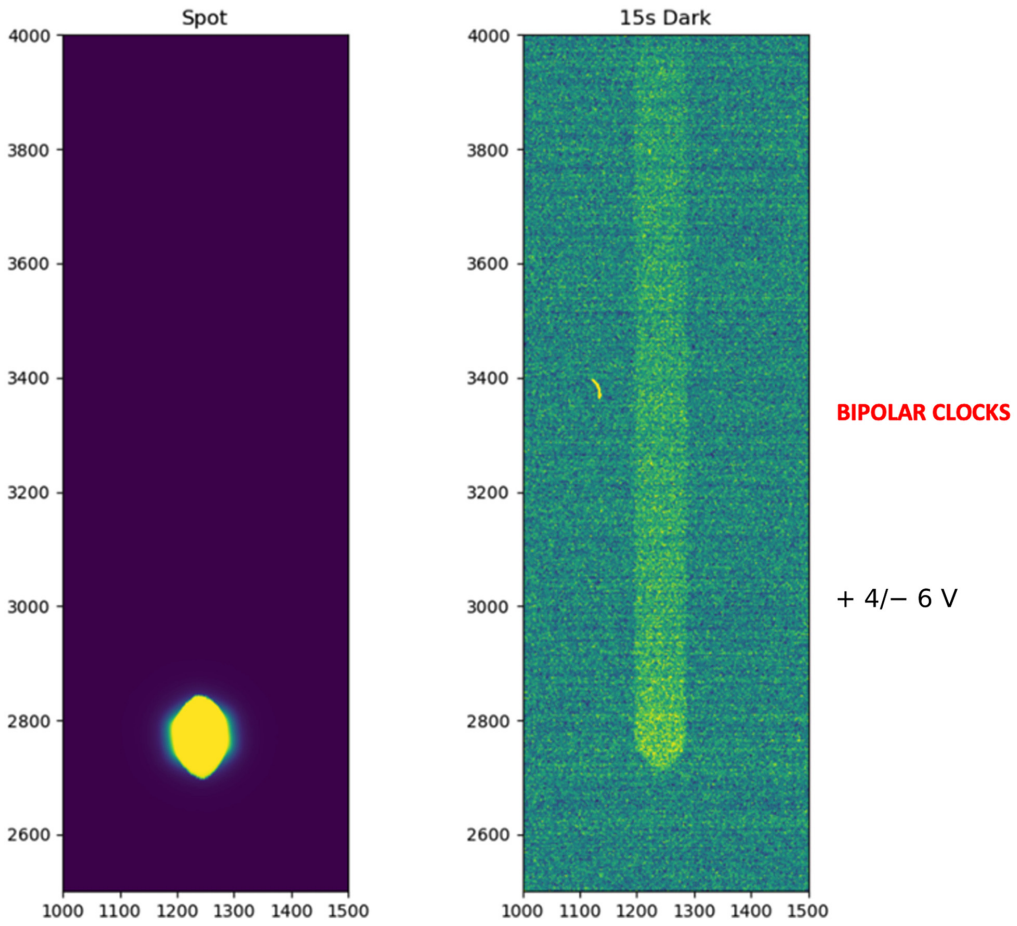

Fig. 10 Teledyne-e2v CCD bright image persistence that is caused by charge trapping during both image integration and readout. Parallel transfer is in the upward direction. LSSTCam Teledyne-e2v CCDs exhibit a range of persistence; the single Teledyne-e2v CCD in our beam simulator has less than the average.

the surface layer is filled by holes.[31] Such a layer of holes can recombine with the excess charges, which eliminates the persistence signal.

Residual images of bright stars in subsequent LSST exposures would create bogus faint galaxies, each with a faint tail in the readout direction. These ghost galaxies will be sheared in the Y-direction (along the column in the previous CCD exposure). In addition to adding a cosmic shear bias (and shear noise), these ghost objects will appear in the image-differencing process used in the alerts pipeline for transient objects. There is no obvious way of mitigating this in instrument signature removal in data processing. One possible mitigation is at the catalog level: filter out objects at the positions of bright stars in the previous exposure.

5 Summary

In this paper, we outline some science drivers for the LSSTCam specifications, particularly those of the CCDs. Laboratory investigations which can lead to an understanding of these effects are as follows:

- Injection: Artificial video signal injection to narrow down the origin of the systematic; does it arise in the CCD chip or in the readout electronics?
- Cable length: Which of the linear and non-linear crosstalk components is affected by cable length? This will give us a hint to separate out the origin of each crosstalk component.
- Overlapping and non-overlapping parallel clocking: Could parallel clocking have an impact on the trailing persistence?

- Lower parallel clock voltage rails: Persistence could be eliminated by a thin population of holes that would recombine with excess charges.
- Narrower parallel clock voltage swing: This would let charges flow along the column direction before getting trapped by the interface.

The residual systematics induced by the CCDs may be mitigated by observational or analysis techniques. These include camera rotation and correction for the brighter–fatter effect in data instrument signature removal. Studies of CCD-based systematic errors that can limit the LSST science reach are undertaken with a hardware LSST beam simulator at UC Davis.[33,34] Some understanding of the parameter space has led to recommendations for optimization of CCD voltages and clocking. These studies are continuing.

Code and Data Availability

Due to the high dimensionality of the optimization search, only a sparse sampling of data was saved. The images and any derived data products presented in this paper are available through a Butler repository[28] hosted by the LSST Data Facility (USDF). Image processing and scientific analyses were done using the LSST Science Pipelines (https://github.com/lsst/cp_pipe, https://github.com/lsst/ip_pipe) developed by Rubin Data Management.[35]

Acknowledgments

This paper has undergone internal review by the Rubin Observatory project. We acknowledge the helpful discussions with Peter Doherty, Claire Juramy, Pierre Antilogus, Steve Ritz, Paul O'Connor, and Aaron Roodman. We also thank two anonymous reviewers for their helpful comments. A.T., C.L., and A.S. were partially supported by the Department of Energy (DOE) (Grant No. DE-SC0009999) and the National Science Foundation (NSF) (Grant No. AST-2205095). This material is based upon work supported in part by the NSF through Cooperative Agreement 1258333 managed by the Association of Universities for Research in Astronomy, and the DOE (Contract No. DE-AC02-76SF00515) with the SLAC National Accelerator Laboratory. Additional LSST funding comes from private donations, grants to universities, and in-kind support from LSSTC institutional members.

References

1. Ž. Ivezić et al., "LSST: from science drivers to reference design and anticipated data products," *Astrophys. J.* **873**(2), 111 (2019).
2. B. Abolfathi et al., "The LSST DESC DC2 simulated sky survey," *Astrophys. J. Suppl. Ser.* **253**(1), 31 (2021).
3. P. A. Abell et al., "LSST science book, version 2.0," arXiv:0912.0201 (2009).
4. P. Marshall et al., "Science-driven optimization of the LSST observing strategy," arXiv:1708.04058 (2017).
5. H. Zhan and J. A. Tyson, "Cosmology with the Large Synoptic Survey Telescope: an overview," *Rep. Prog. Phys.* **81**(6), 066901 (2018).
6. D. J. Bacon, A. R. Refregier, and R. S. Ellis, "Detection of weak gravitational lensing by large-scale structure," *Mon. Not. R. Astron. Soc.* **318**(2), 625–640 (2000).
7. N. Kaiser, G. Wilson, and G. A. Luppino, "Large-scale cosmic shear measurements," arXiv preprint astro-ph/0003338 (2000).
8. D. M. Wittman et al., "Detection of weak gravitational lensing distortions of distant galaxies by cosmic dark matter at large scales," *Nature* **405**(6783), 143–148 (2000).
9. L. Van Waerbeke et al., "Detection of correlated galaxy ellipticities from CFHT data: first evidence for gravitational lensing by large-scale structures," *Astron. Astrophys.* **358**, 30–44 (2000).
10. M. Takada and B. Jain, "The three-point correlation function in cosmology," *Mon. Not. R. Astron. Soc.* **340**(2), 580–608 (2003).
11. T. Eifler et al., "Combining probes of large-scale structure with COSMOLIKE," *Mon. Not. R. Astron. Soc.* **440**(2), 1379–1390 (2014).
12. A. Nicola, A. Refregier, and A. Amara, "Integrated approach to cosmology: combining CMB, large-scale structure, and weak lensing," *Phys. Rev. D* **94**(8), 083517 (2016).
13. Z. Zhang et al., "Transitioning from stage-III to stage-IV: cosmology from galaxy × CMB lensing and shear × CMB lensing," *Mon. Not. R. Astron. Soc.* **514**(2), 2181–2197 (2022).

14. R. Mandelbaum et al., "The LSST Dark Energy Science Collaboration (DESC) Science Requirements Document," arXiv:1809.01669 (2018).
15. M. Yoon et al., "Constraints on cosmology and baryonic feedback with the deep lens survey using galaxy–galaxy and galaxy–mass power spectra," *Astrophys. J.* **870**(2), 111 (2019).
16. M. J. Jee et al., "Cosmic shear results from the deep lens survey. II. Full cosmological parameter constraints from tomography," *Astrophys. J.* **824**(2), 77 (2016).
17. C. Chang et al., "A unified analysis of four cosmic shear surveys," *Mon. Not. R. Astron. Soc.* **482**(3), 3696–3717 (2019).
18. D. R. Neill et al., "Baseline design of the LSST hexapods and rotator," *Proc. SPIE* **9151**, 91512B (2014).
19. H. Almoubayyed et al., "Optimizing LSST observing strategy for weak lensing systematics," *Mon. Not. R. Astron. Soc.* **499**(1), 1140–1153 (2020).
20. M. P. Lesser and J. A. Tyson, "Focal plane technologies for LSST," *Proc. SPIE* **4836**, 240–246 (2002).
21. V. Radeka et al., "LSST sensor requirements and characterization of the prototype LSST CCDs," *J. Instrum.* **4**(03), P03002 (2009).
22. C. Lage, "Physical and electrical analysis of LSST sensors," arXiv:1911.09577 (2019).
23. C. Lage, A. Bradshaw, and J. A. Tyson, "Measurements and simulations of the brighter-fatter effect in CCD sensors," *J. Instrum.* **12**(03), C03091 (2017).
24. P. Antilogus et al., "The brighter-fatter effect and pixel correlations in CCD sensors," *J. Instrum.* **9**(03), C03048 (2014).
25. A. Broughton et al., "Mitigation of the brighter-fatter effect in the LSST camera," *Publ. Astron. Soc. Pac.* **136**(4), 045003 (2024).
26. A. Bradshaw et al., "Mapping charge transport effects in thick CCDs with a dithered array of 40,000 stars," *J. Instrum.* **10**(4), C04034 (2015).
27. A. Tyson et al., "LSST optical beam simulator," *Proc. SPIE* **9154**, 915415 (2014).
28. T. Jenness et al., "The Vera C. Rubin Observatory data butler and pipeline execution system," *Proc. SPIE* **12189**, 1218911 (2022).
29. P. Antilogus et al., "ASPIC: LSST camera readout chip. Comparison between DSI and C&S," in *Top. Workshop on Electron. for Particle Phys. (TWEPP-09)* (2009).
30. P. O'Connor, "Crosstalk in multi-output CCDs for LSST," *J. Instrum.* **10**(05), C05010 (2015).
31. J. R. Janesick, *Scientific Charge-Coupled Devices*, SPIE Press, Bellingham, Washington (2001).
32. P. E. Doherty et al., "Electro-optical testing of fully depleted CCD image sensors for the Large Synoptic Survey Telescope camera," *Proc. SPIE* **9154**, 915418 (2014).
33. Y. Ustumi et al., "LSST camera focal plane optimization," *Proc. SPIE* **13103**, 131030W (2024).
34. A. Snyder et al., "Electro-optical characterization of LSST Camera CCDs using the LSST beam simulator," *Proc. SPIE* **13103**, 1310321 (2024).
35. J. Bosch et al., "An overview of the LSST image processing pipelines," *Astron. Soc. Pac. Conf. Ser.* **523**, 521 (2019).

Biographies of the authors are not available.